REMOTE: RECONNAISSANCE AND MONITORING OF TSUNAMI EVENTS

Frank C. Lin[1*], Kingkarn Sookhanaphibarn[1], Virulh Sa-yakanit[2], George Pararas-Carayannis[3]

[1]Multimedia Intelligent Technology Laboratory
School of Science and Technology, Bangkok University
Rama 4 Rd, Khlong Toei, Bangkok 10110, Thailand.

[2]Center of Excellence in Forum for Theoretical Science
Department of Physics, Faculty of Science, Chulalongkorn University
Bangkok 10330, Thailand

[3]Tsunami Society International, Honolulu, Hawaii 96815, USA

ABSTRACT

The present study describes a prototype we built and named REMOTE for detecting and monitoring in real time tsunami events, based on changes in infrared radiation emitted from the sea when up thrust crustal movements from a major or a great tsunamigenic earthquake disturb the ocean floor and change the thermal properties of the water column in the source region. Specifically, we describe the hardware and software components of this system and present its performance results from recent tsunamis. Declouding of satellite images is often required and this is accomplished by the application of wavelet analysis. Also, in the present study we address the problem of signal delay due to the satellite scanning cycle and discuss possible solutions. Finally, we enumerate the relative benefits of our system. Our proposed system is available to all the countries with access to a geostationary weather satellite.

Corresponding author. Email:linbfrank@gmail.com. Tel/Fax: +662 612 4705.

1. INTRODUCTION

Tsunami(s) are a series of destructive ocean waves usually generated by major or great earthquakes along zones of tectonic subduction where tectonic plates collide. By far, the most destructive tsunamis are caused by large, shallow earthquakes with epicenter or fault line near or on the ocean floor. Displacements of the earth's crust along a rupture resulting from such large earthquakes, lift up the water and generate tsunami waves that can travel across the ocean spreading destruction along their path. Similar displacements of the ocean floor by volcanic eruptions, submarine avalanches, submarine landslides, rock falls and even asteroids can also generate tsunamis. In deep water, tsunamis are characterized by relatively low amplitude, usually less than one meter, but their wavelengths can be hundreds of kilometers long. Thus a tsunami cannot be felt aboard ships in deep water.

In order to mitigate destruction and loss of lives once a tsunami is generated, it is important to have an effective warning system to inform the population in vulnerable coastal areas to evacuate to designated safe zones at higher elevations. The purpose and rationale of the present paper is to assist in such disaster mitigation efforts by providing in real time an alternative and inexpensive method for the early detection and monitoring of a potentially destructive tsunami.

Present methods of detecting and measuring tsunamis in near real time, include coastal tide gauges as well as bottom gauges, such as the "Deep-Ocean Assessment and Reporting of Tsunami" (DART), which essentially measure aquatic pressure changes when a tsunami wave reaches them. The DART system functions as follows: Pressure sensors are placed on the ocean bottom near known earthquake zones. Each deep-water station is equipped with an acoustic modem transducer, which encodes the data into sound waves. An anchored, communications buoy on the ocean surface processes the information and sends it by radio waves to a weather satellite (GOES). Based on such transmitted data, computers at ground stations provide estimates of the tsunami's source region as well as estimates of its wave speed and arrival times at different coastal areas. However, hydrostatic pressure changes recorded by a DART gauge may not be necessarily triggered by a tsunami and, consequently, there are high rates of false alarms. According to Gonzalez [1999] and others, approximately 75% of all warnings issued between 1948 and 1999 were false. Of course, during the early time period, there were no DART stations and in the 90's there were only a few installed and their technology was still under development. The present performance of DART stations has improved since 1999. In this present paper we present a direct, novel and more economical method than DART, which promises, in conjunction with the earthquake detection, to give nearly unequivocal results on detection of tsunami generation.

The main question addressed by the present study is the following: If an undersea earthquake has been detected, by the USGS, the Japan Meteorological Agency or another earthquake monitoring organization, how can it be conclusively determined if a tsunami was indeed generated by this

earthquake? The present study answers this question positively and illustrates how with proper methodology and processing of data from an infrared geostationary satellite, the generation of a tsunami can be detected and monitored. However, at present, we do not account for the propagation of the tsunami, only for its detection and approximate dimensions of the generating source region.

In previous communications [Lin *et al.*, 2010; Lin and Sookhanaphibarn, 2011; Lin *et al.*, 2011; Lin *et al.*, 2012] we publicized our discovery that when tsunamis are generated by a large earthquake, there is infrared radiation of circa 11μm which can be detected by a geostationary satellite. In this paper we present a brief overview of our findings. In addition, we add some new results, which confirm our previous findings, as well as some exceptions (the 2010, Bio-Bio event in Chile and the 2011 Ofunato, Japan event of 2011), for which reasonable justifications are given. Furthermore, we discuss in greater detail the problem of defining tsunami magnitude, which cannot be associated with phase space variables and the application of wavelet analysis to de-clouding methodology, using the great 2004 North Sumatra tsunami as an example. Additionally, but to a limited extent, we compare the advantages of our proposed system of tsunami detection vis-à-vis with that of DART. Finally, we describe in detail both the hardware and software system of our REMOTE system so that it can be appraised, analyzed or replicated, in the belief that it will – when universally implemented - mitigate future loss of life and property from the tsunami hazard.

2. METHOD AND DATA

2.1 Hardware Implementation

A PC-based data receiving and processing system is used to implement the REMOTE tsunami early detection system. The system is designed to receive high frequency satellite signals at approximately 1687 MHz, deploying a parabolic antenna, as shown in Figure 1, of 3m diameter. The gain is 33 dB. A sample of the real-time satellite image is shown in Figure 2 below.

Fig. 1: Disk antenna.
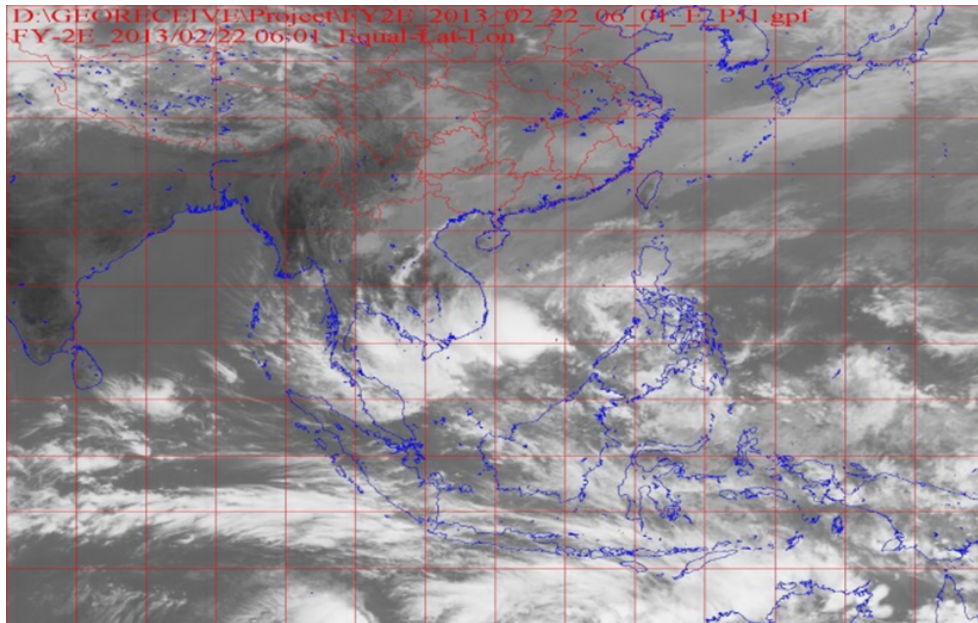
Fig. 2: Real-time satellite image from FY-2E.

The signal from the antenna is fed into a low noise block down-converter (LNA) which is a combination of low-noise amplifier, frequency mixer, local oscillator and IF (Inter-mediate Frequency) amplifier. The LNA switches the signal to an intermediate frequency of 137.5 MHz, which can then be transferred indoors. A receiver in turn converts this to a second intermediate frequency signal of 10.7 MHz. The bandwidth of the receiver is 1.5 MHz and the gain is greater than or equal to 70 dB. After filtering, amplifying and demodulation, the fundamental band signal of 660 kbps is generated. This band signal is further processed by a bit synchronizer for clock extraction and code conversion, and a frame synchronizer for frame synchronous signal detection, channel separation and data format conversion. Finally, these data are input into the 2 PCs (Front end and back end) via a PCI ingestor card, which serves as an interface device, for software processing. A flow diagram for the hardware portion of our system is shown in Figure 3.
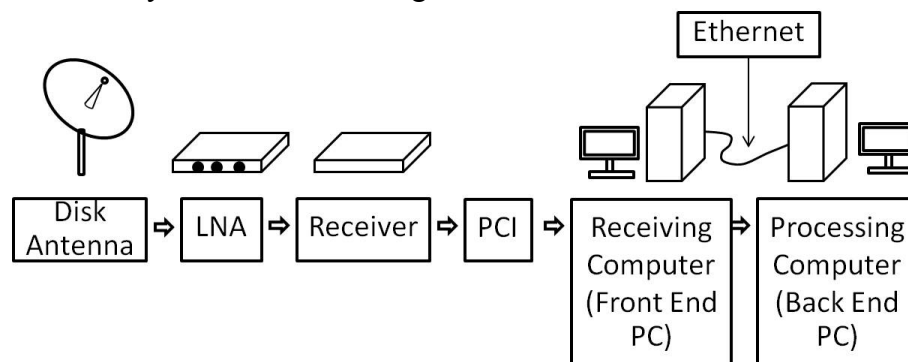
Fig. 3: Flowchart of the hardware portion of REMOTE system.

The front end PC is in charge of data ingesting, viewing, map projection and ftp transfer of the geostationary satellite data (Digital Video Broadcast). The back end PC performs the functions of displaying the image and creating animations and applications. The viewing part of the DVBS displays the channel image in RGB and the scan line information at the title bar. Also, it draws the latitude and longitude grid, political boundaries and geographical features on the image. The IR channel data of each scan line has 2291 scan points, only half of which are displayed on the screen at one time. Five different projection types can be selected. The observation range of the geostationary satellite extends 60 degrees from the Sub-Satellite Point (SSP). The resolution of the IR channel is 5 km. This resolution is adequate for the detection of tsunamis, since the extent of the tsunami signal at the ocean surface is usually 10 to 20 km (two pixels or more). A smaller size of projection image is possible.

The back end PC is mainly an image processing and sub-function producing unit. It has the capability to perform many functions, such as detecting edges, setting palettes, adjusting colors, overlaying maps and contours, etc. It can also add grids, maps, communication lines, and other GIS information. Generated sub-functions include Cloud Cluster Area, Typhoon Location, Precipitation Estimation, Sea Surface Temperature, Outgoing Long Wave Radiation, etc. For our prototype we have directly installed our software in the back end PC. Other options, such as using an Ethernet connection, are possible.

2.2 Software Implementation

Once the satellite image is made available, it is necessary to analyze the image to ascertain whether a tsunami has occurred and, if affirmative, a tsunami warning must be sent to potentially vulnerable areas. A prompt and unambiguous warning sent to the relevant Civil Defense Authorities can save many lives. We describe below the software that we have developed for this purpose. This software can be used in real time in conjunction with the hardware described above, or it can be used independently to analyze historical events. The fundamental physics involved is our observation - as reported in several publications previously - that a tsunami generates an infrared radiation of circa 11 μm (900 cm^{-1}), which can be detected by a geostationary satellite in the infrared domain.

We have implemented the software in MATLAB. The flow diagram for this process is shown in Figure 4 [Lin *et al.*, 2013].

INPUT FILE 1
Satellite Image

INPUT FILE 2
Reference Point

MAIN
PROGRAM

READ
INPUT FILE 1+2

Calculate Pixel Value
of Submarine
Earthquake

Extract
Signal Diagram

Wavelet Diagram
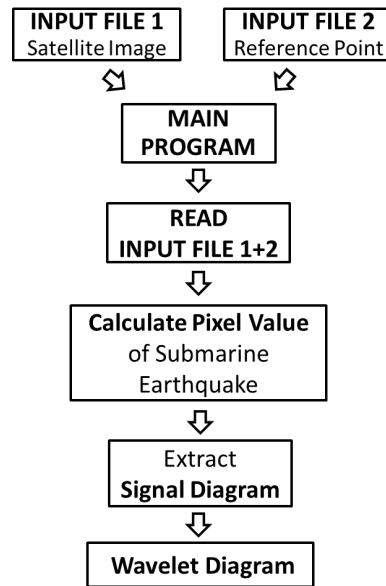
Fig. 4: Processing flowchart of REMOTE system.

In the historical mode, the software reads in the satellite image and two arbitrary reference points whose geodetic positions are known. It calculates the pixel value of the position of submarine earthquake using an interpolation procedure. Then it extracts the Signal Diagram from the satellite image, from which the Wavelet Diagram follows. In the real time mode, this process is continuous and automatic. If a tsunami signal is recognized, a warning is immediately issued. The delay from the time of the submarine earthquake and the tsunami warning is typically minutes.

The following program lines illustrate how the Signal Diagram is extracted from the satellite image:

Algorithm 1:
begin
    load($JPGfilename, Ytsunami, Xtsunami$)
    $imageDat$ =imread($JPGfilename$)
    $rowDat$ = imageDat($Ytsunami$; :)
    $columnDat$ = imageDat(:; $Xtsunami$)
    return($rowDat, columnDat$)
  end

Here, $rowDat$ is the latitudinal Signal Diagram and $columnDat$ the longitudinal Signal Diagram. Y ; $Xtsunami$ are the coordinates of the earthquake epicenter, and $JPEGfilename$ refers to the satellite image.

The Signal Diagrams are then plotted in *Algorithm 2*:

Algorithm 2:
begin
   x=1:length(*rowDat*)
   y=1:length(*columnDat*)
   plot(*x, rowDat*, 'grid on') and title('East-West Signal Diagram')
   plot(*y, columnDat*, 'grid on') and title('North-South Signal Diagram')
   Finally, the Wavelet Diagram is constructed.
end
*Copyright: Kingkarn Sookhanaphibarn and Frank C Lin.

The flow chart of the integrated REMOTE (Reconnaissance and Monitoring of Tsunami Events) system is shown in Figure 5.

Satellite ⇨ Antenna ⇨ Receiver ⇨ Computer ⇨ Visualization ⇨ Monitoring ⇨ Alarm

Earthquake Event
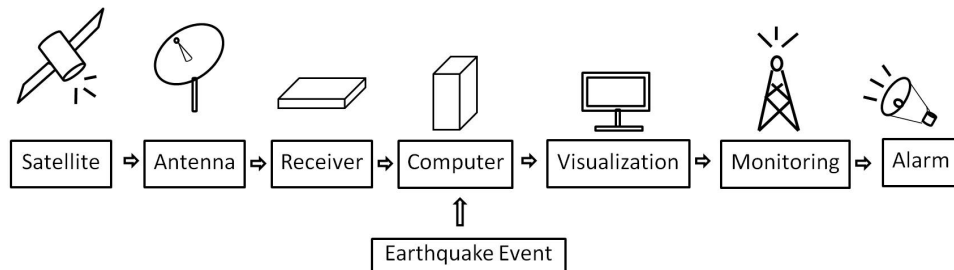
Fig. 5: REMOTE (Reconnaissance and Monitoring of Tsunami Events) flowchart.

3. RESULTS

In the following section we compile a catalogue of recent tsunamis and apply our methodology to evaluate them in order to identify as well as to understand the source origin of tsunamis in infrared space. Our study complements the knowledge gained from the DART system and in particular empowers us to devise a new, satellite-based, early warning system, which responds instantaneously when a tsunami is generated. Specifically, we show the following: 1) A tsunami emits infrared radiation at circa 11 μm; 2) This radiation, called the tsunami signal, can be detected by a geostationary satellite in the infrared domain; 3) This radiation is capable of penetrating extensive cloud cover, which can be demonstrated using the denoising properties of wavelet analysis; 4) The half-life of the tsunami signal is about half an hour and its spatial extent is about 10-20 km; 5) The time delay between the submarine earthquake and the broadcasting of the tsunami by the satellite is typically within minutes; 6) There are no false positives or false negatives (with one exception); and 7) The vector representation of tsunamis in phase space and in infrared space can be mapped into each other by a linear transformation [Lin and Sookhanaphibarn, 2011].

Table 1 shows the Earthquake Magnitude and the tsunami signal, S (see Section IV).

Table 1: Recent Tsunami Events.

Location	Lat.	Long.	Date and Time (UTC) (yy-mm-dd hh:mm:ss)	Me	S pixels
Sumatra	3.3	95.8	2004-12-26 00:58:53	9.0	417
Tohoku	38.3	142.4	2011-03-11 05:46:24	9.0	255
Chile	35.8	72.7	2010-02-27 06:34:00	8.8	170
N.Sumatra	2.31	93.0	2012-04-11 08:38:37	8.6	203
Philippines	10.8	106.8	2012-08-31 12:47:34	7.6	210

3.1 The 2004 Sumatra-Andaman (Banda Aceh) Tsunamigenic Earthquake

On Dec. 26, 2004 a gigantic tsunami in the Indian Ocean was triggered by the subduction of the Indian plate beneath the Burma plate near the Indonesian city of Banda Aceh. The India Plate meets the Burma Plate (which is a portion of the Eurasian Plate) at the Sunda Trench. At this point the India Plate subducts beneath the Burma Plate, which includes the Nicobar Islands, the Andaman Islands and northern Sumatra. According to the USGS, the northern section of the Sunda megathrust, which had been established as a seismic gap, ruptured - the rupture having a total length of 1,300 km. An inspection of the thermal profile of the Indian Ocean shows that the water temperature decreases from around 25 degrees at the surface to about 5 degrees one kilometer below and eventually attaining 4 degrees ten kilometers below. At the onset of tsunami event generation, the sudden crustal movements of the ocean floor caused by the earthquake lift cold water up to the surface. The tsunami burst is therefore characterized by a sudden temperature gradient, which in turn triggers the emission of a thermal tsunami signal. Meteorological satellites such as the Chinese FY-2C, which is geostationary on the earth's equator at Longitude $105°$ and recording wavelengths ranging between 3.5 and 12.5 μm, are able to detect this change in infrared domain. For this particular Chinese satellite, the temperature resolution is 0.5 K and the space resolution is 5 km.

In Figure 6 we show the tsunami signals, i.e. the infrared radiation detected by the FY-2C (also called the pixel brightness when referring to the satellite image), along the latitude of Banda Aceh, at 7 A.M. and 8 A.M. local time, respectively. Because of the temperature gradient of the thermo cline, we expect that the tsunami signal will show up in the latter figure but not in the former.
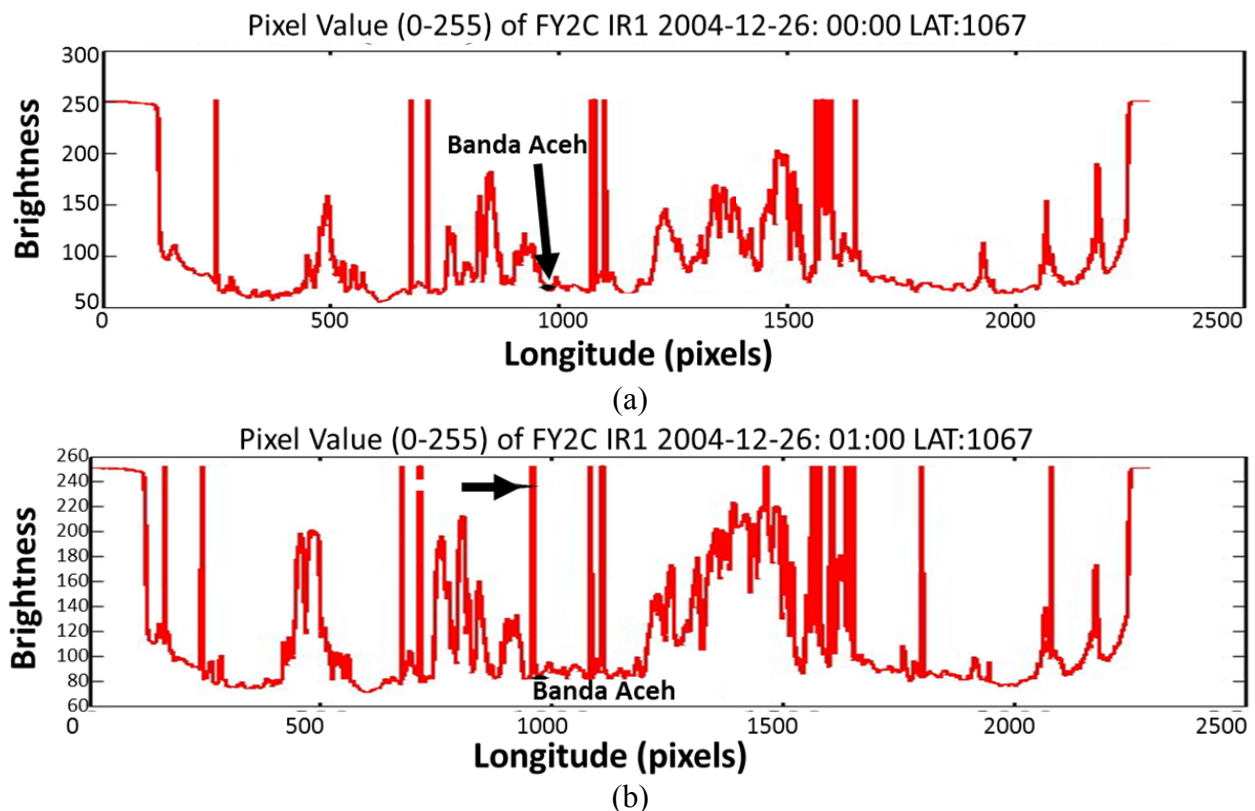
Fig. 6: Signal along Latitude 1067 pixels (latitude of Banda Aceh) at a) 7.00 A.M. and b) 8.00 A.M.

Comparison of Figure 6a and Figure 6b shows that at the location of Banda Aceh, a very strong signal appears at 8 A.M. local time (pointed to by an arrow in Figure 6b), which is absent at 7 A.M. (Figure 6a). Given the time and the location of the spike, there is no doubt that this is the anticipated tsunami signal. We emphasize again that the time and the location define a unique point in four-dimensional space-time with x, y, z, t coordinates (Minkowski space). There is only one spike which satisfies these criteria. In the Signal Diagrams and the Wavelet Diagrams, the tsunami signal is located at the longitude of the submarine earthquake origin. ***All other spikes cannot be attributed to the tsunami signal, since they originate at longitudes where no submarine earthquakes occurred at this point of space-time.***

(a)

(b)

(c)

(d)
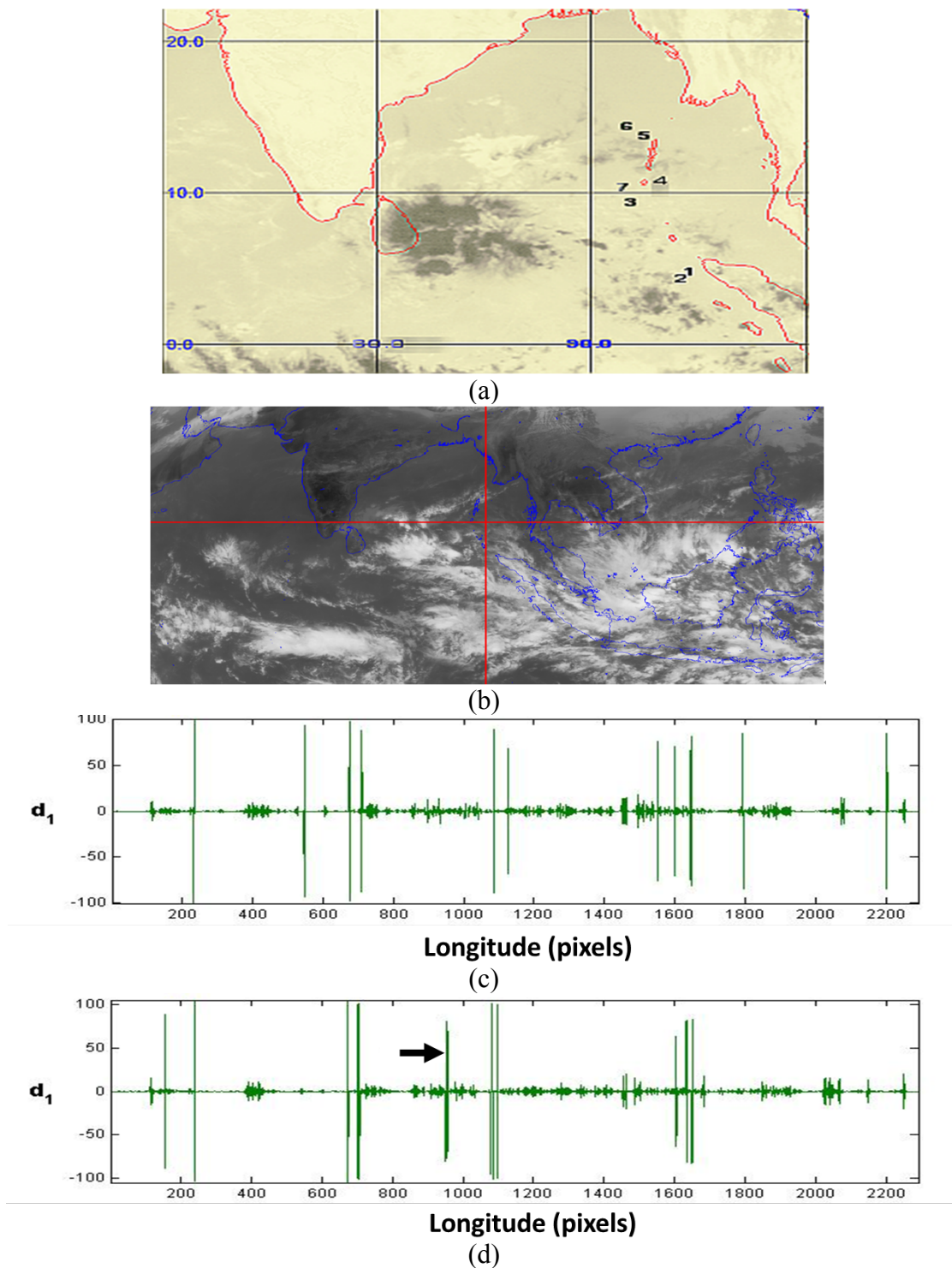
Fig. 7: Aftershocks in Sumatra-Andaman (Banda Aceh) region: a) Location of aftershocks; b) Satellite photo of epicenter for ANDAMAN-Location 2 at 08:00 A.M.; c) Detailed decomposition of the aftershock signal at 09:00 A.M. and d) at 10:00 A.M., respectively.

Figure 7a, shows the locations of the main shock (Position 1) and of some of the subsequent aftershocks (Positions 2 to 7). A satellite image of the Indian Ocean is shown in Figure 7b. It is noteworthy that except for positions 5 and 6 surrounding the Andaman Islands, a tsunami signal is sighted in all other cases, indicating that the colder water from the bottom of the ocean reached the surface and, consequently and unambiguously, a tsunami had been generated - although no flooding at nearby land areas has yet been recorded. In particular, a strong aftershock at location 2 occurred an hour later at the same latitude. Figures 7c and 7d show the Wavelet Diagrams of this event at 9 A.M. and 10 A.M. respectively. In Figure 7c, (9 A.M.) no tsunami signal is seen at the earthquake epicenter, whereas a tsunami signal is distinctly visible in Figure 7d (10 A.M.), as pointed by an arrow. Wavelet analysis is particularly appropriate since it is capable of denoising the satellite images without appreciable degradation.

3.2 The 2011 Tohoku Tsunamigenic Earthquake

On Friday, March 11, 2011 at 05:46:24 UTC (02:46:24 P.M., local time) a great earthquake with a moment magnitude of 9.0 occurred at a depth of 30 km, about 129 km east of Sendai Island of Honshu in Japan. The quake epicenter was at 38.297°N and 142.372°E near the zone of subduction where the Pacific plate moves westward, descending beneath Japan. As a result of this earthquake the coast of northeast Japan moved eastward by about 4 meters and the coastline generally subsided by up to 1.1 meter. The great Tohoku-Oki earthquake - as it was named - generated a very destructive and anomalously high tsunami with a distinct source mechanism [Pararas-Carayannis, 2013]. According to the USGS, the total slip of the quake was approximately 300 km long and 150 km wide. At least 15,703 people lost their lives and at least 332,395 buildings were destroyed or damaged by the combined impact of the earthquake and tsunami along the entire east coast of the Island of Honshu. The maximum tsunami run-up height was 37.88 m at Miyako, very similar to that caused by the 1896 tsunami generated by the Great Tohoku earthquake [Pararas-Carayannis, 2013]. The economic loss in Japan from the 2011 disaster was estimated to be more than 300 billion in U.S. dollars.

In the present study we have systematically investigated the main shock of this event as well as the foreshock and four major aftershocks with the help of the methodology that we have developed and described. The results are summarized in Table 2 [Lin *et al.*, 2011; Lin *et al.*, 2012]. The quantity S in Table 2 represents the tsunami magnitude (Section IV).

Table 2: Tohoku Earthquake - Foreshock and major aftershocks.

Event	Me	Date and Time (UTC) (yy-mm-dd hh:mm)	Lat.	Long.	S pixels	Mt
Main-shock	9.0	2011-03-11 05:46	38.30N	142.37E	255	7.99
Foreshock	7.2	2011-03-09 02:45	38.42N	142.64E	197	7.62
Aftershock-1	7.1	2011-04-07 14:32	38.25N	141.64E	161	7.33
Aftershock-2	6.6	2011-04-11 08:16	37.01N	140.48E	none	N/A
Aftershock-3	7.9	2011-03-11 06:15	36.27N	141.14E	255	7.99
Aftershock-4	7.7	2011-03-11 06:25	38.05N	144.59E	none	N/A

The main conclusions of the present investigation about this event are as follows:

(1) The foreshock on 2011-3-9 had a moment magnitude of 7.62. In the wavelet diagram in Figure 8, a strong tsunami signal is shown as pointed to by an arrow. This foreshadowed the main shock that followed on 2011-3-11. It might have been possible to predict the nucleation and subsequent occurrence of the main shock by using a non-linear forecasting technique such as the Back-propagation Neural Network [Lin and Mohamed, 1999; Lin *et al.*, 2002].

(a)

(b)
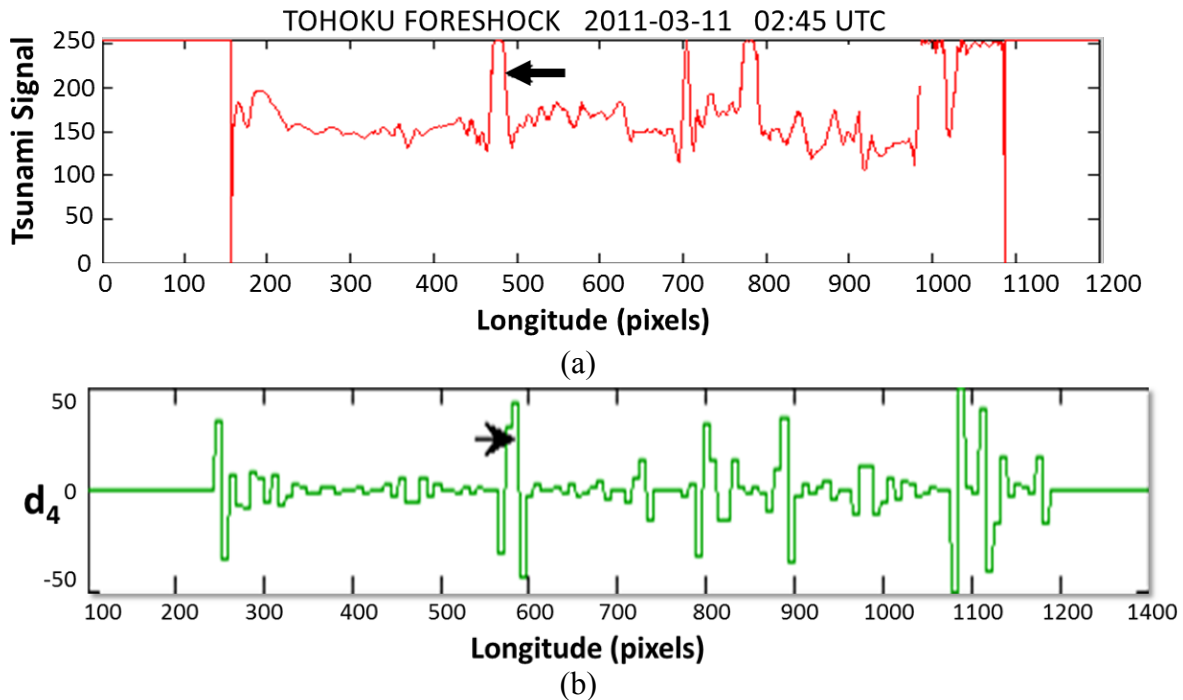
Fig. 8: Tohoku Foreshock event of 2011-3-9: a) Signal Diagram; b) Wavelet Diagram.

(2) The results obtained by remote sensing correlate with and are synchronized with the DART data. In Figure 9, we show the Wavelet diagrams for the main shock, aftershock-3 and aftershock-4, all of which occurred on the same day. Also shown are the readings from DART buoy #21418, which was closest to the tsunami source region. It is seen from Figure 9 that both the main shock and aftershock-3 were registered by the DART buoy, as indicated by the arrows. However, the satellite data did not show a tsunami signal for aftershock-4 and similarly, the DART buoy did not register an earthquake for aftershock-4. There was no spike for afterschock-4.
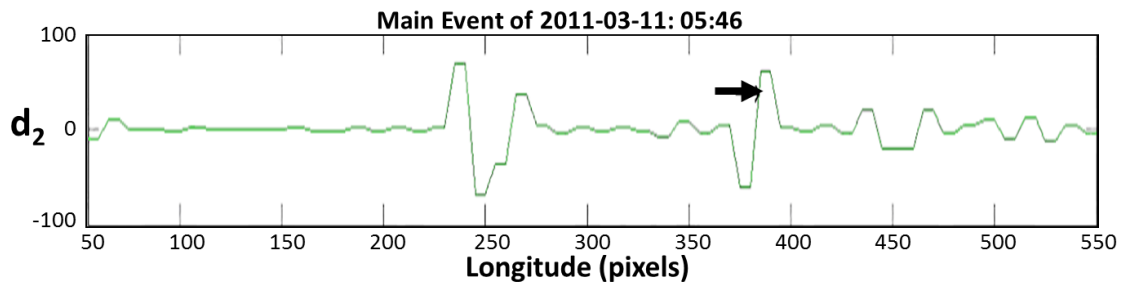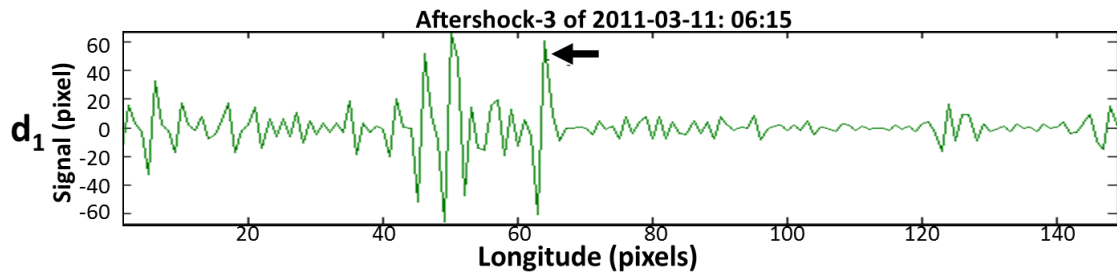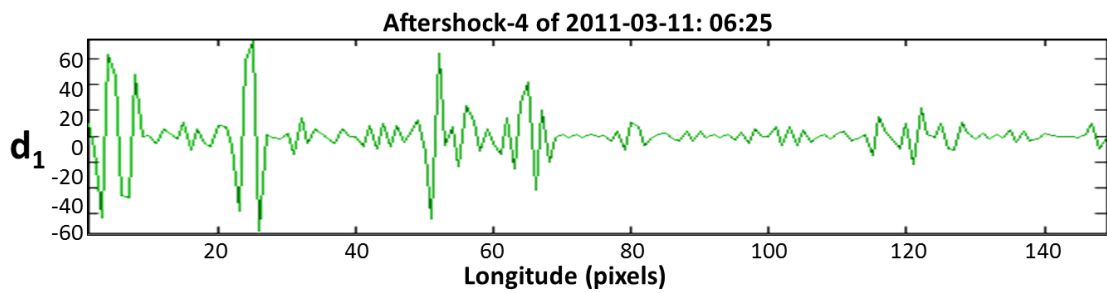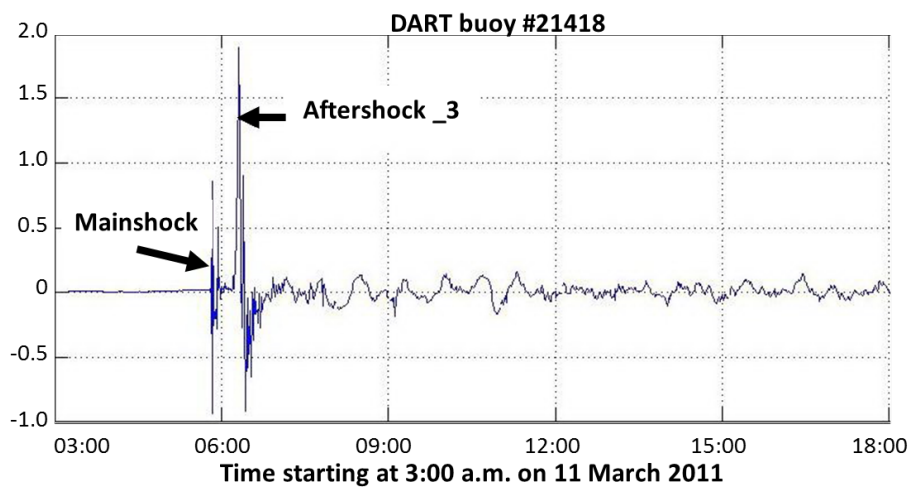
Fig. 9: Satellite data compared with DART data.

Within one hour after the earthquake the tsunami reached the Fukushima Daiichi Nuclear Power Plant, which consists of six boiling water reactors. A maximum 15-meter high tsunami wave easily overflowed the plant's 6-meter protective seawall. The nuclear facility was not prepared for such an emergency and a partial meltdown occurred at reactors #1 and #3. Subsequently, a fire and an explosion at reactor #4 released radioactivity directly into the atmosphere.

3.3 The 2010 Chile BIO-BIO Tsunamigenic Earthquake

On February 27, 2010 an 8.8 magnitude earthquake occurred at 06:34 UTC. Its epicenter was at 35.8°S and 72.7°W, approximately 115 km north of Concepciòn, Chile. The earthquake was triggered by a thrust-faulting focal mechanism occurring at the high rate of 6.8 centimeters per year along an active, oblique subduction zone where the Nazca tectonic plate thrusts below South America. This was the 6th most powerful earthquake in recorded history and the largest in the region since the extremely destructive May 22, 1960 magnitude 9.5 earthquake near Valdivia. In Valparaiso, a tsunami wave of 1.29 m was reported. In spite of the severity of the earthquake, only 525 people lost their lives due to the combined impact of the earthquake and tsunami.

Using GPS data, it was determined that Concepciòn moved at least 3 meters to the west. This movement may have had consequences on the hydrodynamics of the rising cool water following the earthquake. A satellite image taken on 2010-02-27 at 06:39 UTC by GOES-12 is shown in Figure 10a. The blue lines are latitudes and longitudes and the red line delineates the coast of Chile. A flag (white space with x, y pixel values) designates the epicenter of the earthquake. Figure 10b shows the latitudinal (a slice of the satellite image showing the distribution of the pixel brightness along the latitude of the epicenter) Signal Diagram. The spikes pointing downwards are the longitudinal lines.

According to the USGS the epicenter of the earthquake was about 3 km off the coast of Pelluhue commune in the Maule Region. Since the resolution of the satellite image is approximately 5 km, it was not possible to separate the coastline (shown in red in the satellite image) from the tsunami signal. Therefore, it is very likely that the upward spike in the Latitudinal Signal Diagram is a composite of the red coastline and of the tsunami signal.

The Longitudinal Signal Diagram, which is a slice of the Satellite Image along the longitude of the epicenter, is shown in Figure 10c. The position of the earthquake epicenter is marked by a flag. Again, it was not possible to distinguish the tsunami signal from the coastline. The difficulty is attributed to the fact that the earthquake affected a smaller ocean area very close to the shoreline.

Also noted is that while the earthquake took place at 06:34, the satellite image was taken at 06:39, just 5 minutes later. This should not present any difficulty since – according to our estimate - only 2 minutes would have been required for the colder water to reach the ocean surface when the tsunami was generated.
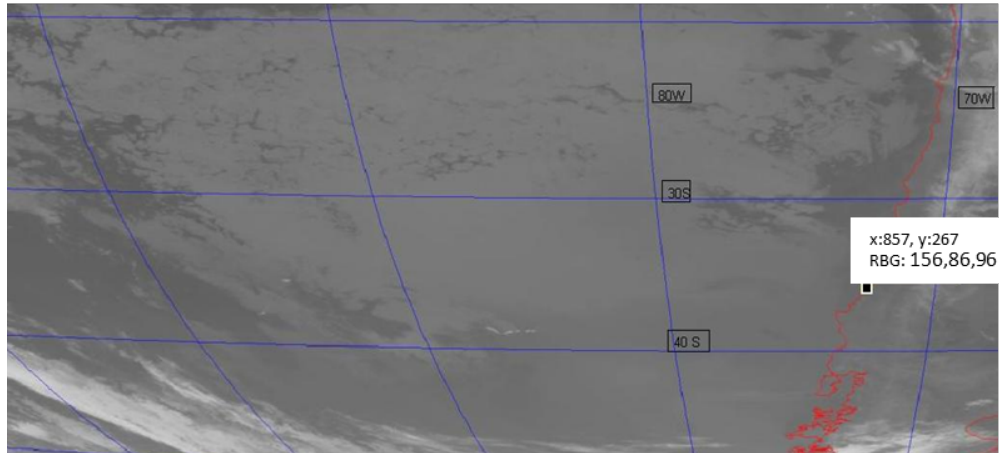
(a)
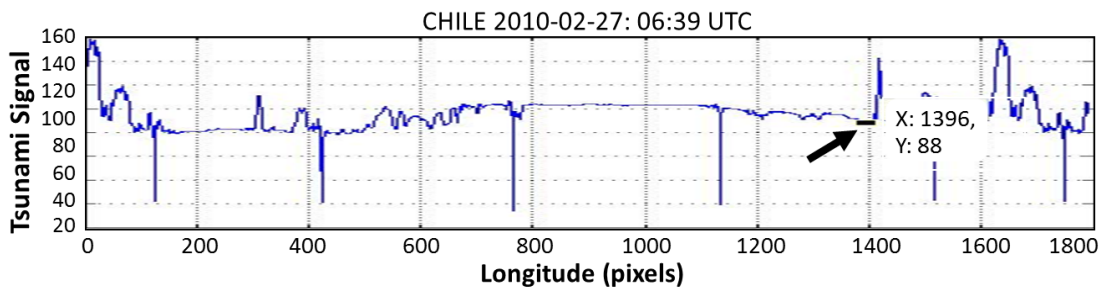
(b)
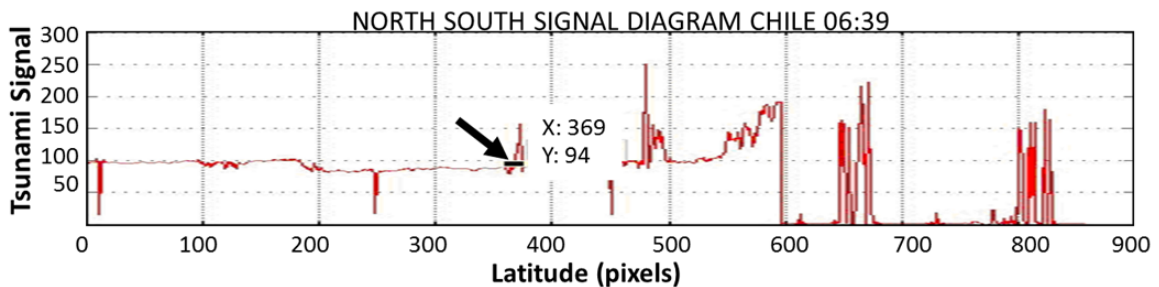
(c)

Fig. 10: Chile Bio-Bio earthquake event: a) Satellite image, b) Latitudinal Signal Diagram and c) Longitudinal Signal Diagram.

Additionally, in explaining the discrepancy, it should be mentioned that although it only takes about 4 minutes to receive a complete GOES image, the raw data reprocessed by NOAA before retransmitting it on 1691 MHz as WEFAX (Weather Facsimile) had a possible delay of about twenty minutes. The discrepancy of a recognizable tsunami signal reception could be due to this delay in transmission, as well as to the extreme land proximity of the submarine earthquake. Furthermore, it is

possible that the tectonic crustal movements affected the hydrodynamics of the rising water in this particular region and that the colder water deflected away from the ocean surface. Such deflection would be expected to have an influence on the strength of the thermal tsunami signal. However, further geological evidence may be needed to explain the signal anomaly for this particular event.

3.4 The 2012 Ofunato, Japan Tsunamigenic Earthquake

On December 7, 2012 at 08:18:24UTC another earthquake with moment magnitude 7.3 occurred east of Sendai, Japan. Its epicenter was at 37.9°N and 143.9°E and its focal depth was 36.1 km. The USGS reported that the earthquake resulted from reverse faulting within the oceanic lithosphere of the subducting Pacific plate moving west northwestward beneath Hokkaido and northern Honshu, Japan. A tsunami warning was issued immediately after the earthquake. A maximum wave of about 1 meter in height reached the Ayukawa district of Ishinomaki at 6:02 P.M. local time, but no casualties were reported.
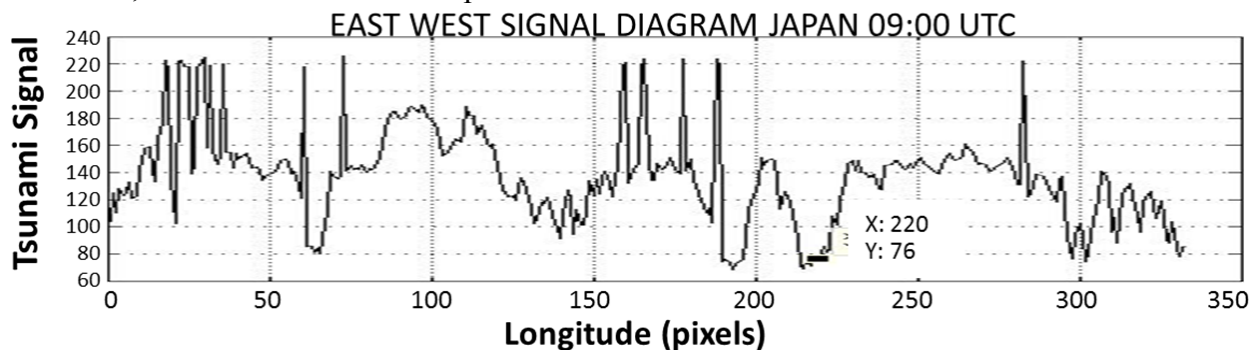
Fig. 11: Latitudinal Signal Diagram for Ofunato, Japan.

Figure 11 shows the latitudinal Signal Diagram taken at 09:00 UTC by MTSAT. At the location of the submarine earthquake, as marked by a flag, there is no evidence of tsunami signal. Since forty minutes elapsed between the earthquake and the satellite infrared exposure, the tsunami thermal signal would have been expected to have decayed. Curiously however, a radiation sink appears to be at the earthquake epicenter at that time.

In order to reduce the blind interval when the satellite image is being refreshed, it is possible to retain multiple geostationary satellites, such as the MTSAT-2 (which takes about 30 minutes to complete a scan) in addition to the FY-2x, whose periods do not overlap for the Asia-Pacific region. Furthermore, in case of an emergency when a strong submarine earthquake has been detected, the scanning interval can be reduced to 10 minutes instead of the customary 30 minutes, as implemented by the Russian satellite Elektro-L. This satellite is stationed over the Indian Ocean at 76°E longitude and can image the entire Earth hemisphere. Its resolution in the infrared band is 4 km. Sensor data downlink to ground uses an X-band (7.5 GHz.) frequency and offers data rates of up to 15.36 Mbits/s.

3.5 The 2012 Sulangan, Philippines Tsunamigenic Earthquake

On 2012-08-31 12:47:34 UTC an earthquake with moment magnitude of 7.6, epicenter at 10.8°N and 106.8°E and a focal depth of 34.9 km occurred 96 km east of Sulangan, Philippines. According to the USGS, this earthquake was an intraplate event, which resulted from reverse faulting within the oceanic lithosphere in the region between the Philippines Sea plate and the Sunda plate. Tectonically, the Philippine Sea plate is bounded by the larger Pacific and Eurasian plates and the smaller Sunda plate. At the latitude of the earthquake, the Philippines Sea plate moves west northwestward at a velocity of approximately 10 cm/year with respect to the Sunda plate.
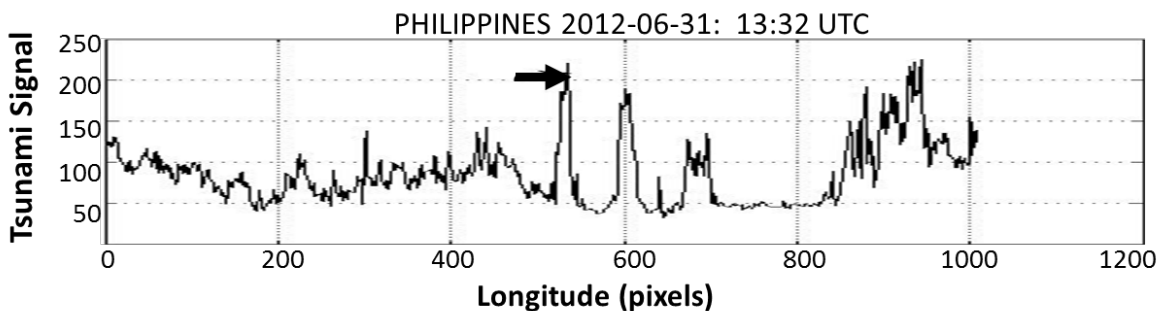
Fig. 12: Latitudinal Signal Diagram for Sulangan, 2012-08-31: 13:32.

Figure 12 shows the Latitudinal Signal Diagram taken by MTSAT on 2012-08-31 at 13:32 UTC. As pointed to by an arrow, the thermal tsunami signal is readily identifiable at the location of the earthquake. According to local authorities, about two hours after the quake, a series of small waves ranging up to 50 centimeters in height, struck the shores of the eastern Philippine Islands, but without causing major damage. There was a report of only one death from a landslide.

3.6 The 2012 Northern Sumatra Events

Clouds whose radiation in the infrared range may not be distinguishable from the tsunami signals frequently cover the world oceans. This constitutes the main source of noise in the detection of tsunamis by the described remote sensing method of the present study. However, it is possible to suppress this noise with an appropriate application of wavelet analysis. We show how utilizing as example the Northern Sumatra tsunami that occurred in 2012 can do this. The parameters of these two tsunami events are given in Table 3.

Table 3: Parameters of the Northern Sumatra Tsunamis of 2012-04-11.

Event	*Me*	Time (UTC)	Lat.	Long.	Thermal Signal at epicenter, pixels	*Mt*
Main-shock	8.6	08:38	2.31	93.0	203	7.665
Aftershock	8.2	10:43	0.77	92.4	138	7.108

For the case of the Aftershock in Table 3, the location of the submarine earthquake marked by a flag on the satellite image is shown in Figure 13a. The Chinese Meteorological Satellite FY-2E on 2011-4-11 captured the historical satellite image in Figure 13a immediately after the seismic events. The red lines are land boundaries; the blue lines are latitudes and longitudes. White patches outside the land mass are clouds over the ocean.

FY-2E 2011-04-11 11.01 UTC

x:508, y:541
RBG: 176,176,176

(a)

(a)

(b)
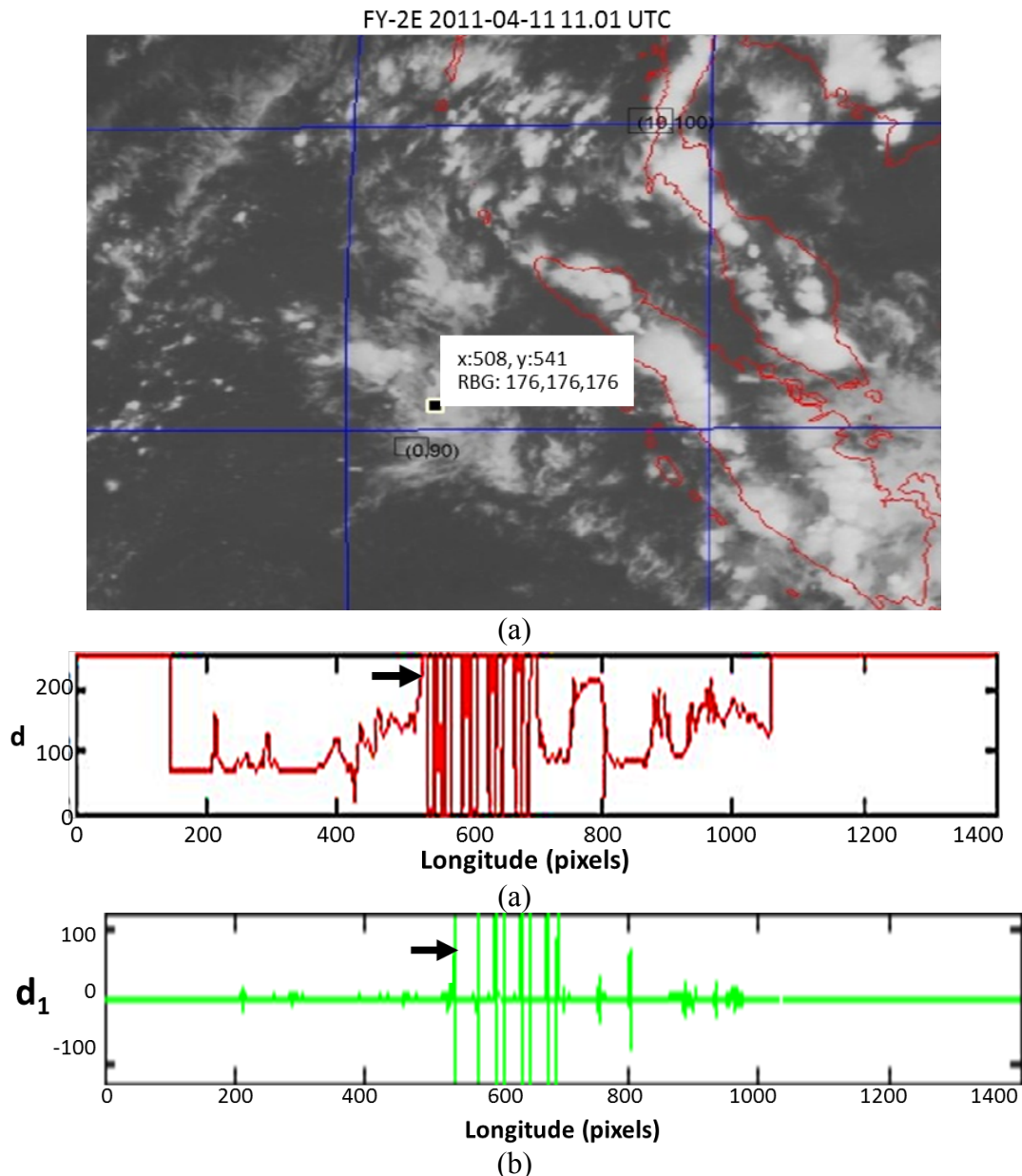
Fig. 13: North Sumatra aftershock at 11:01 UTC; a) Satellite image, b) Signal Diagram and c) Wavelet Diagram.

It is seen that while the cloud in the Signal Diagram, illustrated in Figure 13b, obscures the tsunami signal it is clearly distinguishable in the Wavelet Diagram, shown in Figure 13c. An arrow points to the location of the submarine earthquake. We observe that in Figure 13b the arrow points not to a sharp spike as we would expect from a tsunami signal, but to a block of closely packed, adjacent signals extending between 2 notches. This block is the superposition of the tsunami signal with the infrared radiation emanating from the cloud, which hovers over the location of the earthquake's epicenter. The white patches that are not over land mass - which is demarcated by red boundaries in the mapped image – are due to radiation from the cloud. It is seen from the satellite image that extensive cloud cover covers the location of the submarine earthquake. In the Wavelet Diagram the tsunami signal is clearly visible as a sharp spike at the location of the submarine earthquake. As mentioned earlier, this is because wavelet analysis can compress or denoise a signal without appreciable degradation. Also, it is possible that a cloud cover can be so dense that no infrared radiation can penetrate it. However, this does not happen very often. For instance, in the Indian Ocean during the monsoon season, the clouds are carried by the wind at considerable speed, so that any single cloud does not stay at one location long enough to obscure the tsunami signal.

Another source of noise is the infrared radiation emitted by the adjacent land mass. However, we can easily recognize its origin by comparing the satellite image with a topographic map. Regarding the horizontal scale, all Signal Diagrams encompass 500 pixels between notches and all Wavelet Diagrams span 200 pixels between notches unless otherwise labeled. For the vertical scale, the range of Signal Diagrams is from 0 to 250 and the range for Wavelet Diagrams is from -100 to +100, unless otherwise labeled.

4. DISCUSSION

In order to be able to assess the damage that can be caused by a tsunami and issue a warning as to the severity of its anticipated impact, it is useful to define a measure of tsunami magnitude and relate it to the severity of the submarine earthquake that generated it. In phase space, Iida *et al*. [Iida, 1958; Iida *et al*., 1967] defined the tsunami intensity by:

$$It = log2(\sqrt{2} \times S) \tag{1}$$

Where S is the estimated maximum run-up height of the wave. The logarithmic function is convenient, as in the case of the Richter scale, to compress the numerical values into a narrow range. This measure has also been suggested based on the effect and damage caused by the tsunami. In the following we shall consider three possible definitions of tsunami magnitude in infrared space. The Tsunami Magnitude, the Tsunami Index, and the Tsunami Coefficient. In analogy to equation (1), we define the *Tsunami Magnitude*, *Mt* as follows:

$$Mt = log2S \tag{2}$$

where Mt is *Tsunami Magnitude* and S represents *Tsunami Signal* (Pixel brightness at the epicenter. See Table 1 for numerical values obtained directly from the satellite images). Based mainly on empirical data, Iida *et al*. [Iida, 1958; Iida *et al.*, 1967] found a linear relationship between the Mt and Me in visible space, as follows:

$$Mt = 2.61Me - 18.44 \tag{3}$$
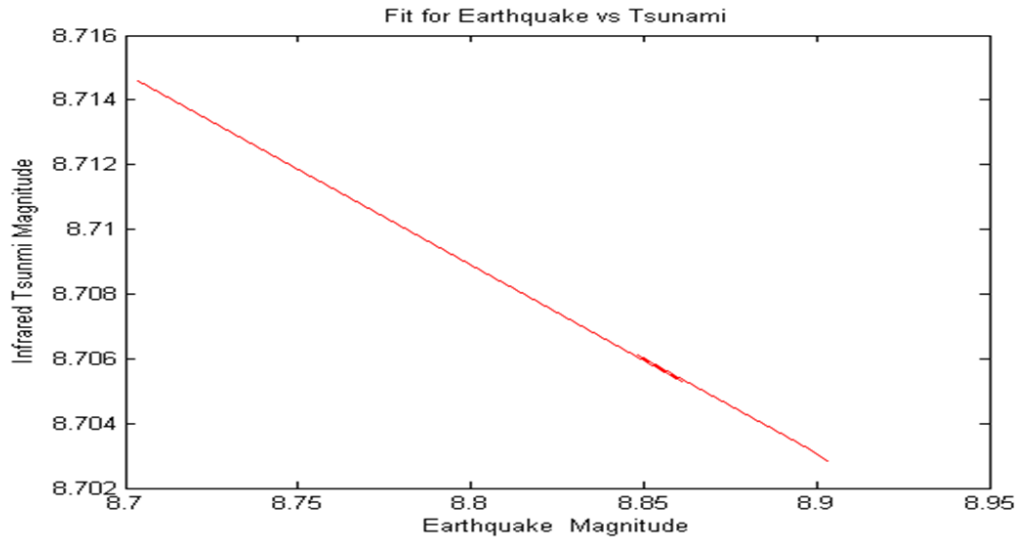
Fig. 14: Infrared tsunami vs earthquake magnitude.

As in the case of Iida *et al.* the earthquake magnitude and tsunami magnitude *in infrared space* also lie approximately on a straight line. The equation for least square fit is given by:

$$Mt = 9.2299 - 0.052Me \tag{4}$$

We observe that the Tsunami Magnitude as we have defined is a decreasing function of the earthquake magnitude as shown in Figure 14. This is probably a manifestation of the negative correlation between temperature and tsunami signal: the lower the temperature of the water, the stronger is the tsunami signal. However, in customary usage, this is counter-intuitive. Intuitively it is useful to regard a measure of tsunami magnitude as an increasing function of the earthquake magnitude. We define a calibrated tsunami magnitude called the *Tsunami Index*, I as follows:

$$I = 1000log2 - 1S - 110 \tag{5}$$

The relationship of I to Me is given in Fig. 15 for Banda Aceh:
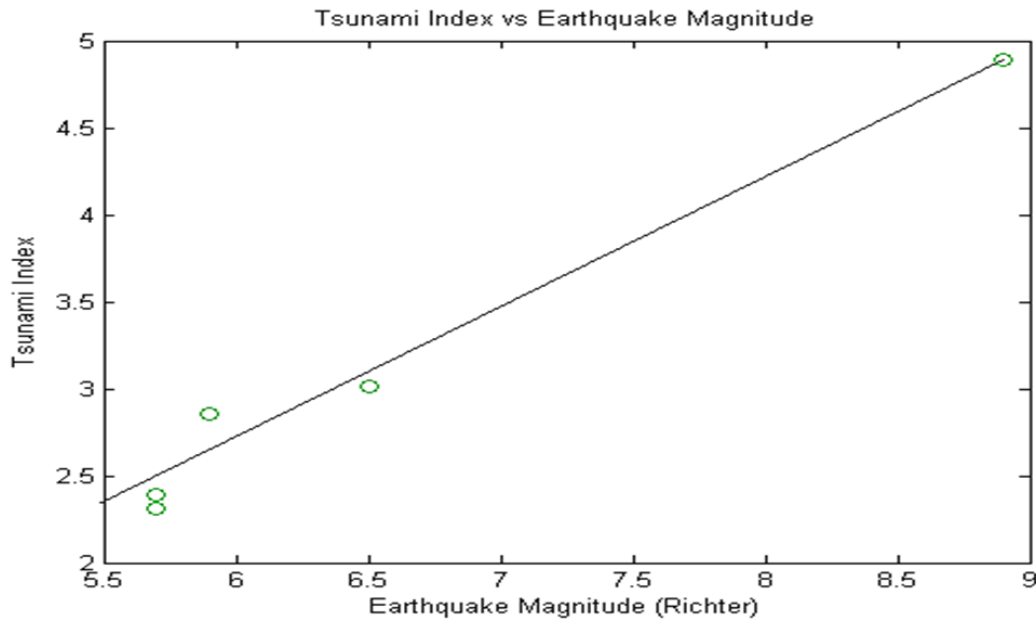
Fig. 15: Earthquake Magnitude (*Me*) vs Infrared Tsunami Index (*I*) at epicenter.

These results can be used to estimate the tsunami magnitude. The 'far point' in Figure 15 is the Main Event. As we have mentioned, there are many factors that contribute to the birth of a tsunami. Since in the range we are considering, the submarine earthquake is a *force majeure* [Lin and Sookhanaphibarn, 2011], other factors such as underwater currents are insignificant in comparison or cancel out.

The strength of a tsunami can also be estimated by the reciprocal of the Tsunami Signal. We define the Tsunami Coefficient, *K* as follows:

$$K = 1000S - 1 \tag{6}$$

An empirical formula between the *Tsunami Coefficient*, *K*, and the *Earthquake Magnitude* is given by equation (7) as follows.

$$K = 0.0922Me - 1.579 \tag{7}$$

from which we can estimate the tsunami strength from the earthquake magnitude, subject to the limitation of the approximations involved. The data points in Fig. 16 are from Banda Aceh. The goodness of fit is: *SSE* = 0.001 and *R-square* = 0.9839. We do not expect the linearity to be perfect, since the ocean floor bathymetric features vary greatly at different locations.
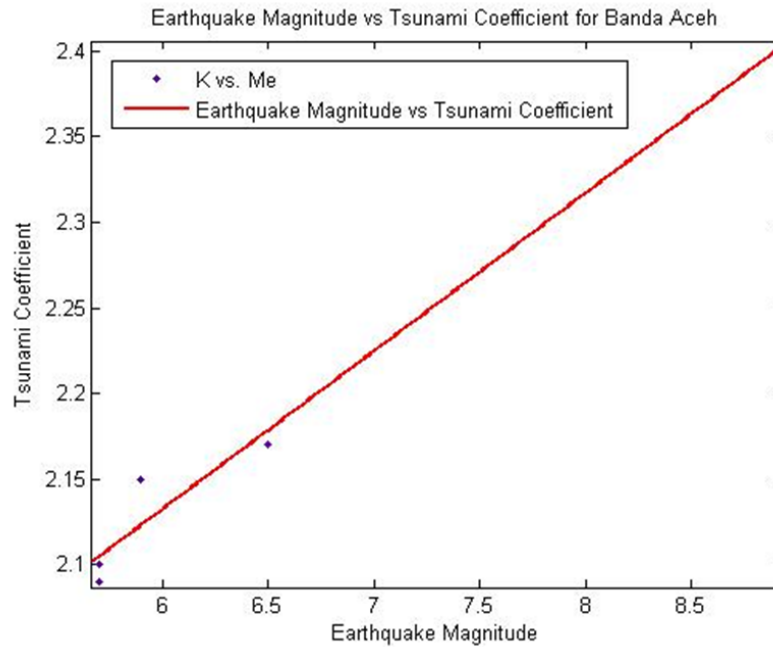
Fig. 16: Tsunami Coefficient (K) vs Earthquake Magnitude (Me).

Table 4: Tsunami Magnitude and Tsunami Coefficient.

Location	Event	Me	Time UTC	S pixels	K	Mt
INDIAN OCEAN	Main- shock	8.9	00:58	417	2.40	8.7
	Aftershock	5.9	02:59	465	2.15	8.9
	Nicobar	6.5	09:20	461	2.17	8.8
	Andaman-1	5.7	07:07	477	2.10	8.9
	Andaman-4	5.7	06:21	479	2.09	8.9
TOHOKU	Main- shock	9.0	05:46	255	3.92	7.9
	Foreshock	7.2	02:45	197	5.08	8.0
	Aftershock-1	7.1	14:32	161	6.21	7.33
	Aftershock-3	7.9	06:15	255	3.92	8.0
N.SUMATRA	Main- shock	8.6	08:38	203	4.92	7.7
	Aftershock	8.2	10:43	138	7.25	7.1

As previously indicated, we have investigated thoroughly the tsunami phenomena in infrared space. Other investigators, such as the MOST model [Titov and Gonzalez, 1997], have made use of variables in phase space. The question that can be posed is: What is the relationship between these two representations? Since both representations stand for the same tsunami, it must be possible to map from one to the other by a mathematical transformation and since the dynamic equations are linear, by

a linear transformation. We construct a generalized hyperspace, in which both the phase space and the infrared space are embedded. The two representations are vectors in this space. We can therefore carry out a linear transformation to map an element from IR to P or vice versa by a rotation and two translations. Thus [Lin and Sookhanaphibarn, 2011]:

$$vp = \mathbf{R} \cdot vIR + \mathbf{T}Me \cdot vIR + \mathbf{T}Mt \cdot vIR \qquad (8)$$

The matrix $\mathbf{R}$ is the usual rotational operator given by:

$$\mathbf{R} = cos\ \varphi - sin\varphi\ 0\ sin\varphi\ cos\varphi\ 0\ 0\ 0\ 1 \qquad (9)$$

where φ is the angle of rotation.

Therefore these representations are equivalent. If any other space is invoked, its elements must satisfy the condition that a linear transformation exists which maps its elements into the canonical representation, in order that the tsunami magnitude is self-consistent with the other representations.

This theorem is supported by experimental data, for instance by satellite data compared with the DART data of 2011-03-11 at Tohoku, as shown in Figure 9.

The quantity S in the Table 4 is the strength of the tsunami signal (pixel brightness). Since the earthquake and the tsunami signal are *causally related*, it could not have been a coincidence that they occupy the same point, i.e. same spatial position and the same time, in Minkowski space. We conclude therefore that the relation between them is not random.

5. CONCLUSION

In a previous communication [Lin *et al*., 2013] we have shown the advantages of the REMOTE system as a satellite based tsunami early warning system. In the following we discuss the performance features of REMOTE from four points of view: Time delay, reliability, cost and availability. In terms of time delay, assuming that the depth of submarine earthquake is 30 km and the velocity of the tsunami is 1000 km/hr, it will take 2 minutes for the tsunami signal to reach the geostationary satellite and a warning broadcasted. *This time lapse is critical for the effectiveness of Early Warning*. In terms of cost, we estimate that the initial cost including hardware and software will be of the order of 10^4 euros and the maintenance cost is minimal. For private entrepreneurs, it is possible to purchase the components of our system via the Internet for a few hundred euros.

For our system, in theory, there are no false positives or false negatives. It is easy to understand this if we consider two cases: 1) The cool water from the bottom of the ocean is dissipated before it reaches the surface. 2) The cool water reaches the surface of the ocean, mixes with warm water, and radiates. In the first case, no tsunami is generated and the satellite did not detect the tsunami signal. It

is a negative event. In the second case, the satellite does receive a tsunami signal and therefore sounds a warning. It is a positive event (In our catalog the Chile Bio-Bio is an ambiguous case due to its unusual topology). In terms of availability, this system can be made available to every country with access to a weather satellite. If implemented, this system should function essentially instantaneously without any margin of error, and should benefit all communities presently threatened by tsunamis, thereby saving life and property.

REFERENCES

M. Arii, M. Koiwa, and Y. Aoki, "Effective monitoring for marine debris after the great east Japan earthquake by using polarimetric SAR data," IGARSS 2013, Melbourne, Australia, Jul. 2013.

E. Bernard and C. Meinig, "History and future of deep-ocean tsunami measurements," in OCEANS 2011, pp. 1-7, 2011.

J.-F. Cayula and P. Cornillon, "Edge detection algorithm for SST images," Journal of Atmospheric and Oceanic Technology, vol. 9, no. 1, pp. 67- 80, 1992.

L. H. Coudert, O. Pirali, M. Vervloet, R. Lanquetin, and C. Camy-Peyret, "The eight first vibrational states of the water molecule: measurements and analysis," Journal of Molecular Spectroscopy, vol. 228, pp. 471- 498, December 2004.

E. L. Geist, V. V. Titov, D. Arcas, S. L. Bilek, and F. F. Pollitz, "Implications of the 26 December 2004 Sumatraandaman earthquake on tsunami forecast and assessment models for great subduction-zone earthquakes," Bulletin of the Seismological Society of America, vol. 97, pp. S249-S270, January 2007.

F. Gonzalez, "Tsunami!," Scientific American, vol. 280, pp. 56-65, 1999.

B. D. Hamlington, R. R. Leben, O. A. Godin, J. F. Legeais, E. Gica, and V. V. Titov, "Detection of the 2010 chilean tsunami using satellite altimetry," Natural Hazards and Earth System Science, vol. 11, no. 9, pp. 2391-2406, 2011.

B. Hamlington, R. Leben, O. Godin, E. Gica, V. Titov, B. Haines, and S. Desai, "Could satellite altimetry have improved early detection and warning of the 2011 Tohoku tsunami?," Geophysical Research Letters, vol. 39, no. L15605, 2012.

K. Iida, "Magnitude and energy of earthquakes accompanied by tsunami and tsunami energy," Journal of Earth Science, vol. 6, no. 2, pp. 101- 112, 1958.

K. Iida, D. C. Cox, and G. Pararas-Carayannis, "Preliminary catalog of tsunamis occurring in the Pacific Ocean," Hawaii Institute of Geophysics, University of Hawaii, 1967.

F. C. Lin and I. E. Mohamed, "Predicting seismic aftershocks using a neural network," in Proceedings of the IEEE 1999 International Geoscience and Remote Sensing Symposium, vol. 2 of IGARSS99, (Munich, Germany), pp. 1366-1368, July 1999.

F. C. Lin, N. Elhassan, A. Hassan, and A. Yousif, "Forecast of seismic aftershocks using a neural network," in Proceedings of the 9th International Conference on Neural Information Processing, 2002, vol. 4 of ICONIP'02, (Singapore), pp. 1796-1799, July 2002.

F. C. Lin, K. n. Nakornphanom, K. Sookhanaphibarn, and C. Lursinsap, "A new paradigm for detecting tsunamis by remote sensing," International Journal of Geoinformatics, vol. 6, no. 1, pp. 19-30, 2010.

F. C. Lin and K. Sookhanaphibarn, "Representation of tsunamis in generalized hyperspace," in Proceeding of the IEEE International Geoscience and Remote Sensing Symposium, IGARSS11, (Sendai/Vancouver), pp. 4355-4358, July 2011.

F. C. Lin, W. Zhu, and K. Sookhanaphibarn, "Observation of tsunami radiation at Tohoku by remote sensing," Science of Tsunami Hazards, vol. 30, no. 4, pp. 223-232, 2011.

F. C. Lin, W. Zhu, and K. Sookhanaphibarn, "A detail analysis of the Tohoku tsunami by remote sensing," in Proceedings of the IEEE International Geoscience and Remote Sensing Symposium, IGARSS12, (Munich, Germany), pp. 1166-1169, July 2012.

F. C. Lin, W. Zhu, P. Silapasuphakornwong, and K. Sookhanaphibarn, "Remote: a satellite based tsunami early warning system," in Proceedings of the IEEE 2013 International Geoscience and Remote Sensing Symposium, IGARSS13, (Melbourne, Australia), pp.3694-3697, July 2013.

G. Pararas-Carayannis, "The Great Tohoku-Oki Earthquake and Tsunami of March 11, 2011 in Japan: A Critical Review and Evaluation of the Tsunami Source Mechanism," Pure and Applied Geophysics, pp. 1-22, 2013.

J. Park, K. Anderson, R. Aster, R. Butler, T. Lay, and D. Simpson, "Global seismographic network records the great Sumatra-Andaman earthquake," Eos, Transactions American Geophysical Union, vol. 86, no. 6, pp. 57-61, 2005.

J. Park, K. Anderson, R. Aster, R. Butler, T. Lay, and D. Simpson, "A catalog of tsunamis in the Indian ocean," Science of Tsunami Hazards, vol. 25, no. 3, pp. 128-142, 2006.

D. B. Percival and A. T. Walden, Wavelet Methods for Time Series Analysis (Cambridge Series in Statistical and Probabilistic Mathematics). Cambridge University Press, Feb. 2000.

V. V. Titov and F. I. Gonzalez, "Implementation and testing of the method of splitting tsunami (most) model," tech. rep., NOAA Technical Memorandum ERL PMEL-112, 11 pp UNIDATA, 1997.

C. E. Synolakis, E. N. Bernard, V. V. Titov, U. Knoglu, and F. I. Gonzlez, "Validation and verification of tsunami numerical models," Pure and Applied Geophysics, vol. 165, pp. 2197-2228, 2008.

P. C. C. Ullman, David S., "Evaluation of front detection methods for satellite-derived SST data using in situ observations," Journal of Atmospheric and Oceanic Technology, vol. 17, pp. 1667-1675, 2000.